



Activated TiO_2 with tuned vacancy for efficient electrochemical nitrogen reduction



Zishan Han^a, Changhyeok Choi^b, Song Hong^a, Tai-Sing Wu^c, Yun-Liang Soo^c, Yousung Jung^{b,*}, Jieshan Qiu^d, Zhenyu Sun^{a,*}

^a State Key Laboratory of Organic-Inorganic Composites, Beijing University of Chemical Technology, Beijing, 100029, People's Republic of China

^b Graduate School of EELS, Korea Advanced Institute of Science and Technology (KAIST), Daejeon, 34141, Republic of Korea

^c Department of Physics, National Tsing Hua University, Hsinchu, 30013, Taiwan

^d State Key Laboratory of Chemical Resource Engineering, College of Chemical Engineering, Beijing University of Chemical Technology, Beijing, 100029, People's Republic of China

ARTICLE INFO

Keywords:

Ammonia
Electrochemistry
 N_2 reduction
Oxygen vacancy
 TiO_2

ABSTRACT

Renewable energy-driven electrochemical N_2 reduction reaction (NRR) provides a green and sustainable route for NH_3 synthesis under ambient conditions but is plagued by a high reaction barrier and low selectivity. To promote NRR, modification of the catalyst surface to increase N_2 adsorption and activation is key. Here, we show that engineering surface oxygen vacancies of TiO_2 permits significantly enhanced NRR activity with an NH_3 yield rate of about $3.0 \mu\text{g}_{\text{NH}_3} \text{h}^{-1} \text{mg}_{\text{cat}}^{-1}$ and a faradaic efficiency (FE) of 6.5% at -0.12 V (vs. the reversible hydrogen electrode, RHE). Efficient conversion of N_2 to NH_3 is achieved in a wide applied potential range from -0.07 to -0.22 V (vs. RHE) with NH_3 production rates $\geq 2.0 \mu\text{g}_{\text{NH}_3} \text{h}^{-1} \text{mg}_{\text{cat}}^{-1}$ and NH_3 FE $\geq 4.9\%$, respectively. An NH_3 FE as high as 9.8% is obtained at a low overpotential of 80 mV. Density functional theory calculations reveal that the surface oxygen vacancies in TiO_2 play a vital role in facilitating electrochemical N_2 reduction by activating the first protonation step and also increasing N_2 chemisorption (relative to ${}^* \text{H}$).

1. Introduction

NH_3 is one of the most demanded value-added chemicals worldwide with wide uses in agricultural fertilizers, drug manufacturing, and industrial raw materials [1]. Industrial-scale ammonia production is heavily reliant on the traditional Haber-Bosch (HB) process invented in the 1900s. The HB process uses fossil fuels and suffers from inherent drawbacks such as high temperature ($> 300^\circ\text{C}$), high pressure ($> 10 \text{ MPa}$) [2], complicated factory infrastructure, enormous energy consumption (over 1% of world's annual energy output), and substantial CO_2 emissions (3 CO_2 per 8 NH_3). Therefore, more sustainable and environmentally friendly alternatives such as biological N_2 fixation (mimicking a natural method of N_2 fixation) [3], electrochemical [4–12], and photochemical [13–18] reduction processes have been developed.

The electrochemical reduction of N_2 powered by electricity from renewable energy sources provides a simple and sustainable way for NH_3 production, involving the reaction of N_2 and H_2O ($\text{N}_2 + 8\text{H}^+ + 6\text{e}^- \rightleftharpoons 2\text{NH}_4^+$ (or 2NH_3)) under mild conditions, yet without feeding H_2 . It also facilitates storage of intermittent renewable energy

in a carbon-neutral fuel (NH_3). The electrochemical N_2 reduction reaction (NRR) often encompasses two steps: the reductive adsorption of N_2 to form N_2H^* (* indicates an active site on the catalyst) with no need to cleave the triple bond in N_2 and the reductive desorption of NH_2^* to yield NH_3 [1]. The first step was suggested to be the rate-determining step for NRR. A superior catalyst should selectively stabilize N_2H^* but destabilize NH_2^* . Thermodynamically, hydrogen evolution reaction (HER) competes with NRR at similar potentials, leading to poor faradaic efficiency (FE) toward NH_3 [19]. Also, a large overpotential is usually needed to promote N_2H^* formation that is kinetically sluggish [20]. Consequently, an optimal catalytic system would be required to suppress the parasitic HER and accelerate NRR at low overpotentials [19].

Engineering catalysts by introducing active defects provides an effective and flexible route to tune catalytic activities [21]. In particular, the creation of oxygen vacancies (V_o) in metal oxides (or hydroxides) can enhance reactant adsorption and activation as well as stabilization of reaction intermediates, thereby affecting catalytic performance for various processes including CO_2 conversion [22–25], oxygen reduction reaction [26,27], and N_2 photofixation [28–31]. However, to our best knowledge, tuning surface oxygen vacancies of catalysts to facilitate

* Corresponding authors.

E-mail addresses: ysjn@kaist.ac.kr (Y. Jung), sunzy@mail.buct.edu.cn (Z. Sun).

NRR has been seldom reported in electrocatalytic NH_3 synthesis. Herein, we report the activation of TiO_2 for efficient NRR to produce NH_3 under ambient conditions by engineering surface oxygen vacancies. Control of annealing temperature makes it possible to readily tune the V_o level of TiO_2 and its catalytic properties for the NRR. An oxygen vacancy-rich TiO_2 can produce an NH_3 yield rate of *ca.* 3.0 $\mu\text{g}_{\text{NH}_3} \text{h}^{-1} \text{mg}_{\text{cat}}^{-1}$ at -0.12 V (vs. the reversible hydrogen electrode, RHE). Notably, an NH_3 FE of over 5.3% can be achieved in a wide potential range from -0.02 to -0.17 V (vs. RHE), substantially outperforming pristine TiO_2 . Density functional theory (DFT) calculations disclose that the surface oxygen vacancies can stabilize $^*\text{NNH}$, which otherwise is a highly destabilized and potential determining reaction intermediate over pristine TiO_2 , hence significantly lowering the free energy for NRR on these defective sites.

2. Experimental

2.1. Reagents and materials

Titanium tetrachloride (TiCl_4 , 99.9%), ethylene glycol (EG, \geq 99%), and DMSO-d_6 were purchased from Aladdin. HCl (37%) was provided by Beijing Chemical Works. NaClO was purchased from Macklin. Nafion membranes were provided by Alfa Aesar. All chemicals were of analytically pure grade and used as received without further treatments. Ultrapure water (18.2 megohm·cm) was obtained by using the Milli-Q Synthesis System. Nitrogen gas (99.999% purity) and argon gas (99.999% purity) were provided by Beijing Haipu Gas Company, Ltd.

2.2. Synthesis of oxygen-vacancy rich TiO_2 nanosheets

Typically, TiO_2 nanosheets with various oxygen vacancies were synthesized *via* a solvothermal process followed by calcination at different temperatures in Ar [27]. The samples annealed at 700, 800, and 900 °C were denoted as $\text{TiO}_2(\text{V}_o)_700$, $\text{TiO}_2(\text{V}_o)_800$, and $\text{TiO}_2(\text{V}_o)_900$, respectively.

Specifically, 1 mL of TiCl_4 and 1 mL of deionized water were added dropwise into 30 mL of EG under vigorous stirring. After stirring for 3 h, the obtained homogeneous solution was transferred into a 50 mL Teflon-lined stainless steel autoclave. The autoclave was sealed and then heated at 150 °C for 4 h before it was cooled to room temperature. The white precipitate was centrifuged and washed thoroughly with deionized water and ethanol, and then dried at 60 °C overnight. After grinding with a mortar and pestle, the as-prepared TiO_2 was annealed in Ar at a specific temperature (700, 800, or 900 °C) for 3 h with a heating rate of 2 °C min⁻¹. The obtained samples were collected for further characterization.

2.3. Characterization

X-ray powder diffraction (XRD) was performed with a D/MAX-RC diffractometer operated at 30 kV and 100 mA with $\text{Cu K}\alpha$ radiation. X-ray photoelectron spectroscopy (XPS) experiments were carried out using a Thermo Scientific ESCALAB 250Xi instrument. The instrument was equipped with an electron flood and scanning ion gun. All spectra were calibrated according to the C 1s binding energy at 284.8 eV. Electron spin resonance (ESR) spectra were obtained using a Bruker e-scan ESR spectrometer (300 K, 9.7397 GHz). Scanning electron microscopy (SEM) was carried out using a field emission microscope (FEI Quanta 600 FEG) operated at 20 kV. High-angle annular dark field scanning transmission electron microscopy (HAADF-STEM) was conducted using a JEOL ARM200 microscope with 200 kV accelerating voltage. STEM samples were prepared by depositing a droplet of suspension onto a Cu grid coated with a Lacey Carbon film. X-ray absorption fine spectroscopy (XAFS) measurements were performed in the fluorescence mode using a Lytle detector at beam line BL07A of Taiwan

Light Source, NSRRC. A Si(111) Double Crystal Monochromator (DCM) was used to scan the photon energy. The energy resolution ($\Delta E/E$) for the incident X-ray photons was estimated to be 2×10^{-4} . Quantitative information on the radial distribution of neighboring atoms surrounding Ti was derived from the extended absorption fine structure (EXAFS) data. An established data reduction method was used to extract the EXAFS χ -functions from the raw experimental data using the IFEFFIT software. To ascertain reproducibility of the experimental data, at least two scans were collected and compared for each sample. Nitrogen and oxygen temperature programmed desorption (N_2 -TPD and O_2 -TPD) measurements were performed on the Micromeritics AutoChem II 2920 apparatus. Prior to the test, the sample was pretreated in a He stream at 150 °C for 1 h with a flow rate of 50 mL min⁻¹ to clean the catalyst surface. After cooling to 50 °C under a He atmosphere, the sample was subjected to adsorption of N_2 or O_2 for 3 h. Then the residual N_2 or O_2 was removed by purging with He for another 0.5 h. The desorption of N_2 or O_2 was then performed by heating at a rate of 10 °C min⁻¹ from 50 to 350 °C. The TPD signal was recorded simultaneously using a thermal conductivity detector (TCD). Infrared data were collected using a Nicolet 6700 ATR-IR spectrometer with a liquid nitrogen-cooled MCT detector. Thermogravimetric (TGA) analysis was performed on a SII TG/DTA 6300 instrument in a N_2 atmosphere.

2.4. Electrochemical measurements

Controlled potential electrolysis of N_2 was tested in an H-cell system, which was separated by a Nafion 117 membrane. Before NRR tests, the Nafion membrane was pretreated by heating in 5% H_2O_2 aqueous solution at 80 °C for 1 h and subsequently in 0.5 M H_2SO_4 at 80 °C for 1 h. Toray Carbon fiber paper with a size of 1 cm \times 1 cm was used as working electrode. Pt wire and Ag/AgCl electrodes were used as counter electrode and reference electrode, respectively. The potentials were controlled by an electrochemical working station (CHI 760E, Shanghai CH Instruments Co., China). All potentials in this study were measured against the Ag/AgCl reference electrode (in 3 M aqueous KCl corresponding to an $E^\circ_{\text{Ag/AgCl}} = 0.205$ V) and converted to the RHE reference scale by

$$E (\text{V vs. RHE}) = E (\text{vs. Ag/AgCl}) + 0.205 + 0.059 \times \text{pH}$$

Electrocatalytic reduction of N_2 was conducted at room temperature (about 25 °C) unless stated otherwise and atmospheric pressure. N_2 (99.999%) was purged into the electrolyte for at least 30 min to remove residual air in the reservoir, then controlled potential electrolysis was performed at each potential for 60 min with N_2 flowing through the cell. During the electrolysis, the electrolyte was stirred with a stirring bar at a stirring rate of about 350 rpm. N_2 regulated by a mass flow controller (Sevenstar Instrument) at 20 mL min⁻¹ flowed through the cell. A flow rate of 20 mL min⁻¹ was chosen to ensure sufficient N_2 transport to the surface while avoiding interference from gas bubbles striking the surface. To ensure reproducibility of catalytic data, we performed NRR tests over TiO_2 catalysts at least three times, each with a new electrode. All potentials reported in this work are with respect to the RHE scale unless specified otherwise.

3. Results and discussion

3.1. Catalyst characterization

The X-ray diffraction (XRD) patterns of as-made catalysts before and after annealing are given in Fig. 1a. The sample before annealing exhibits diffraction peaks at approximately 24.9, 28.2, and 48.6° in trace A, which can be well indexed to the (110), (002), and (020) reflections of monoclinic $\text{TiO}_2(\text{B})$ (β -phase TiO_2) (JCPDS file 046-1237) [32]. Upon annealing at 700 and 800 °C in Ar, $\text{TiO}_2(\text{B})$ was converted to anatase. Both treated samples showed pronounced peaks at 25.3, 37.8, and 48.0° (in traces B and C), corresponding to the (101), (004), and

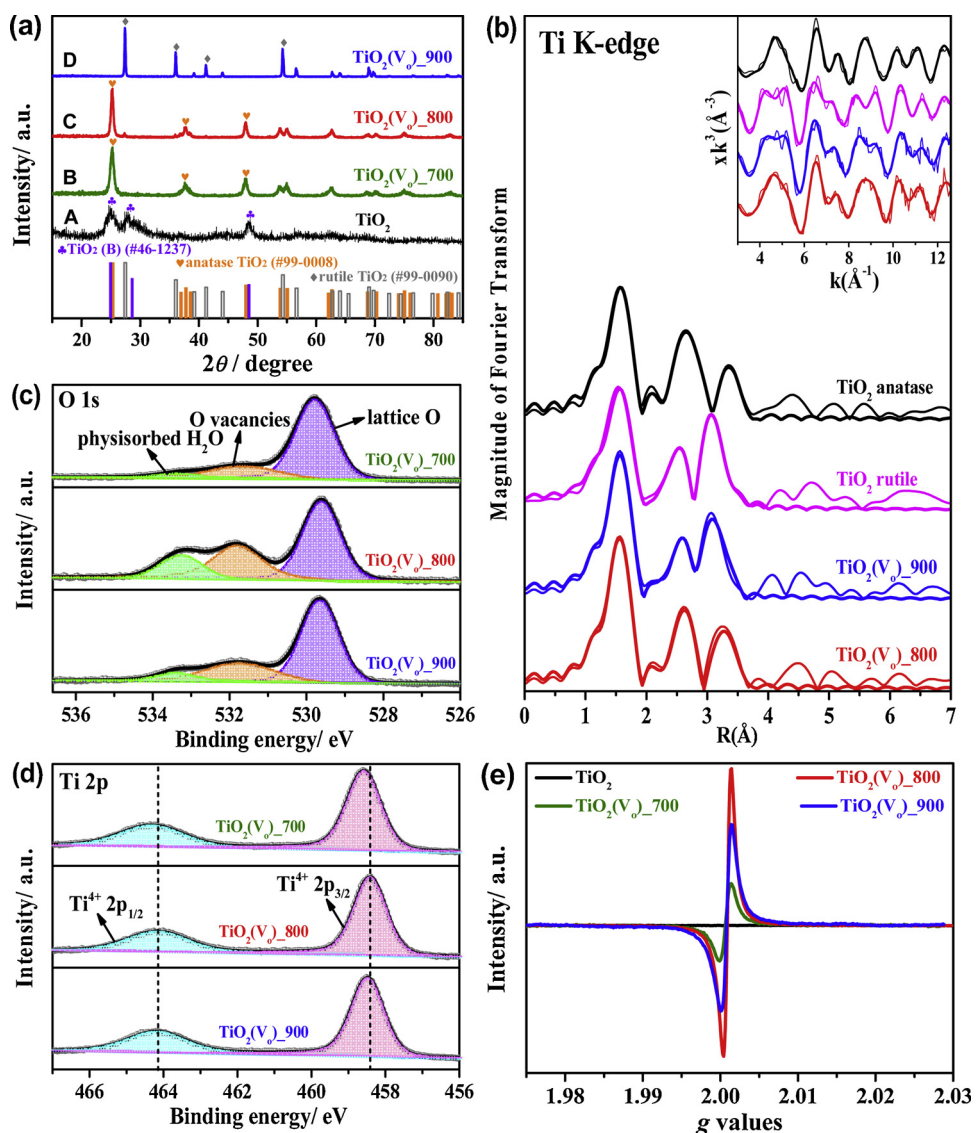


Fig. 1. (a) XRD patterns of pristine TiO₂ (trace A), TiO₂(V_o)₇₀₀ (trace B), TiO₂(V_o)₈₀₀ (trace C), and TiO₂(V_o)₉₀₀ (trace D). (b) Fourier transformed EXAFS spectra of TiO₂(V_o)₈₀₀, TiO₂(V_o)₉₀₀, standard anatase, and rutile TiO₂. The inset in b is Ti K-edge extended EXAFS oscillation function $k^3\chi(k)$. (c) O 1s and (d) Ti 2p XPS spectra of TiO₂(V_o)₇₀₀, TiO₂(V_o)₈₀₀, and TiO₂(V_o)₉₀₀. (e) ESR spectra of pristine TiO₂, TiO₂(V_o)₇₀₀, TiO₂(V_o)₈₀₀, and TiO₂(V_o)₉₀₀.

(200) reflections of tetragonal anatase TiO₂ (JCPDS, 99-0008), owing to crystalline structure conversion from TiO₂(B). The main peak positions of TiO₂(V_o)₈₀₀ are nearly identical to those of TiO₂(V_o)₇₀₀, indicative of the preservation of anatase phase. Whereas in the case of TiO₂(V_o)₉₀₀, phase transformation from TiO₂(B) to rutile occurred with diffraction peaks appearing at 27.4, 36.1, and 54.3° (in trace D), consistent with the (110), (101), and (211) reflections of rutile TiO₂ (JCPDS, 99-0090).

The formation of anatase in TiO₂(V_o)₈₀₀ and rutile in TiO₂(V_o)₉₀₀ was also confirmed by Fourier transformed extended X-ray absorbance fine structure (EXAFS) (Fig. 1b) and Ti K-edge X-ray absorption near-edge structure (XANES) (Fig. S1) analyses. The positions of atomic shells, relative peak intensities, and line shapes of TiO₂(V_o)₈₀₀ and TiO₂(V_o)₉₀₀ match well with the spectral features of standard anatase and standard rutile samples, respectively.

X-ray photoelectron spectroscopy (XPS) measurements were carried out to probe surface composition and chemical state (up to 3 nm in depth) of the TiO₂ catalysts. For all the three annealed samples, the O 1s peaks at 533.3, 531.7, and 529.7 eV are attributed to physisorbed water, O atoms associated with surface Ti–OH species (surface oxygen vacancies for TiO₂ prepared *via* hydrolysis and hydrothermal methods),

and lattice oxygen in TiO₂, respectively (Fig. 1c) [23,33,34]. The large O 1s peak at 531.6 eV for pristine TiO₂ (Fig. S2) can be ascribed to –OH species of adsorbed ethylene glycol (EG) molecules which are difficult to be removed even after repeated washing. The percentage of V_o in surface O species for the catalysts treated at 700, 800, and 900 °C was calculated to be 18.4, 32.2, and 25.6%, respectively, by XPS based on the ratio of the oxygen-vacancy peak area and the total O 1s XPS spectrum area. Clearly, the V_o fraction increases with increasing temperature from 700 to 800 °C but drops at higher temperature 900 °C. This is probably due to the formation of rutile at 900 °C and less favorable generation of V_o in rutile than in anatase [35]. Meanwhile, as compared to TiO₂(V_o)₇₀₀, the Ti 2p_{3/2} and 2p_{1/2} peaks for both TiO₂(V_o)₈₀₀ and TiO₂(V_o)₉₀₀ shifted to lower binding energy (BE) values (Fig. 1d), suggesting decrease in Ti oxidation state. Such occurrence likely arises from the partial reduction of Ti⁴⁺ by localized electrons at oxygen vacancy sites [36]. The TiO₂(V_o)₈₀₀ exhibited lower Ti 2p peak BEs than TiO₂(V_o)₉₀₀ because the former sample has a higher V_o content. We expect that the sample annealed at 800 °C featuring the highest level of surface V_o may provide the most distinct catalytic properties for electrocatalytic N₂ fixation, which will be discussed in the electrochemical results.

O₂ temperature-programmed desorption (TPD) measurements (Fig. S3) showed two pronounced peaks for TiO₂(V_o)₈₀₀, attributable to physically adsorbed (< 200 °C) and chemically adsorbed (between 200 and 400 °C) oxygen species. TiO₂(V_o)₈₀₀ exhibited higher amounts of adsorbed oxygen than TiO₂(V_o)₈₀₀O₂, which can be ascribed to the presence of oxygen vacancies in the former sample. Raman spectroscopy showed broadening and shift of the E_g mode to higher wavenumbers for defective TiO₂ samples (Fig. S4a). This is mostly due to phonon confinement effects caused by localized defects [37]. In addition, the E_g peak shift value was observed to be proportional to the V_o content, following the trend TiO₂(V_o)₈₀₀ > TiO₂(V_o)₇₀₀ > TiO₂(V_o)₈₀₀O₂.

The existence of V_o was further verified by ESR. In stark contrast to pristine TiO₂(B) that shows no ESR peak, the three annealed TiO₂ samples all exhibit a pair of steep peaks with a symmetric distribution (Fig. 1e) in accordance with a V_o signal at g = 2.003, an indication of electron trapping at oxygen vacancies [38]. This unambiguously proved that annealing of pristine TiO₂ in Ar successfully introduced V_o [39]. The presence of bridging surface hydroxyls (i.e., V_o) in annealed samples was also supported by Fourier-transform infrared spectroscopy (FTIR) [33]. A broad band at 3428 cm⁻¹ originating from bridging hydroxyls and/or physisorbed water was observed in all the cases with peak intensity following the sequence TiO₂(V_o)₇₀₀ < TiO₂(V_o)₉₀₀ < TiO₂(V_o)₈₀₀ (Fig. S4b), agreeing well with the trend of the V_o percentage. Furthermore, thermogravimetric analysis (TGA) in Fig. S4c indicated weight losses of 2.2, 1.6, and 0.53% in the temperature range from 373 to 973 K for TiO₂(V_o)₈₀₀, TiO₂(V_o)₉₀₀, and TiO₂(V_o)₇₀₀, corresponding to total V_o (Ti-OH) concentrations of 5.5, 4.0, and 1.33%. In combination with XPS results, we can infer that oxygen vacancies are predominantly on the surface of TiO₂ nanosheets.

Scanning electron microscopy (SEM) (Figs. 2a and S5a) and high-angle annular dark field scanning TEM (HAADF-STEM) (Fig. 2b-d) studies show a large number of flakes with lateral sizes of 20 nm to 1 μm that stack on top of each other. Most of the flakes observed by STEM have a thickness of approximately 15 nm (Fig. 2c). HRTEM observations along with fast Fourier transform (FFT) indicate good crystallinity of the resultant anatase TiO₂ (Fig. 2e). Many bright dots on the flake surfaces were identified, as encased in yellow dashed circles (Fig. 2f), which are likely protruding Ti atoms at oxygen vacancy sites. Structural analysis based on high-resolution STEM image was further carried out to visualize possible defects induced in the TiO₂ samples. Intrinsic bulk defects (variable distances between adjacent lattice fringes) and disordered edges (loss of orientation, as marked with an ellipse in the line-profile of image g, inset of Fig. 2g) were observed. HRTEM images in the bright-field mode also reveal the disordered layers at flake edges possibly induced by oxygen vacancies (Fig. 2h). The formation of TiO₂ was confirmed by EDX (Fig. S5b) together with elemental mapping (Fig. 2i).

3.2. Electrocatalytic reduction of N₂ to NH₃

Linear sweep voltammetry (LSV) measurements were conducted to evaluate the effects of oxygen vacancies in TiO₂ on the catalytic performance for NRR. No obvious difference is observed for pristine TiO₂ after electrolysis in Ar- or N₂-saturated 0.1 M aqueous HCl, indicative of its poor activity for N₂ reduction. In stark contrast, TiO₂(V_o)₇₀₀, TiO₂(V_o)₈₀₀, and TiO₂(V_o)₉₀₀ all show apparently higher current densities under N₂ saturation, implying the occurrence of N₂ reduction (Fig. 3a). It should be noted that TiO₂(V_o)₈₀₀ with the highest V_o content exhibits a significantly larger net current density (J_{N2}-J_{Ar}) [40] than both TiO₂(V_o)₇₀₀ and TiO₂(V_o)₉₀₀ at similar potentials.

We also found that NRR took place at potentials > -0.02 V with an overpotential of ≤ 80 mV (given the equilibrium thermodynamic potential for N₂ reduction to NH₃ is 0.06 V vs. normal hydrogen electrode under our experimental conditions (298 K and 1 atm)) with V_o-rich TiO₂ as a cathode catalyst (Fig. 3b). Under the reaction conditions

adopted, only NH₄⁺ ions were identified by the indophenol blue method (Fig. S6). No N₂H₄ as by-product was detectable by the Watt and Chrisp method [41] within the detection limit of the method. The produced ammonia was also determined by ion chromatography [42,43] and NMR spectroscopy [7,44]. The ammonia yield rate was derived to be about 2.8 (Fig. S7) and 3.0 μg_{NH3} h⁻¹ mg_{cat}⁻¹ (Fig. S8) by ion chromatography and ¹H NMR measurements, respectively, comparable to the value of 3.0 μg_{NH3} h⁻¹ mg_{cat}⁻¹ obtained by the indophenol blue method. Electrolysis was also performed on TiO₂(V_o)₈₀₀ in Ar at -0.12 V, showing nearly undetectable NH₃. This has confirmed that NH₃ evolved is due to the electroreduction of dissolved N₂. The yield rate of NH₃ initially increases before reaching a maximum at -0.12 V and then started to decline with further increasing applied overpotential. Although the NH₃ FE decreases monotonically with increasing applied potential, the FE is still higher than 4.9% in a wide potential range from -0.02 to -0.22 V on TiO₂(V_o)₈₀₀ (Fig. 3c). At all applied potentials, TiO₂(V_o)₈₀₀ surpassed the other catalysts with an NH₃ yield rate of about 3.0 μg_{NH3} h⁻¹ mg_{cat}⁻¹ at -0.12 V, being 2.4, 1.4, and 1.2 times higher than that of pristine TiO₂, TiO₂(V_o)₇₀₀, and TiO₂(V_o)₉₀₀. The TiO₂(V_o)₈₀₀ also exhibited a higher NH₃ FE of up to 6.5% at -0.12 V, in contrast to 2.4, 4.1, and 4.8% for pristine TiO₂, TiO₂(V_o)₇₀₀, and TiO₂(V_o)₉₀₀, respectively. Note that both NH₃ FE (≈ 6.5%) and NH₃ yield rate (≈ 3.0 μg_{NH3} h⁻¹ mg_{cat}⁻¹) of our V_o-rich TiO₂ are higher than those values reported over cathodes of Ru [45], porous Ni [46], MXene nanosheets [10], Pd_{0.2}Cu_{0.8}/reduced graphene oxide [47], and Fe₂O₃/carbon nanotubes [48] under ambient conditions. Likewise, the calculated turnover number (TON) with respect to TiO₂ content for NH₃ formation also follows the order: TiO₂(V_o)₈₀₀ > TiO₂(V_o)₉₀₀ > TiO₂(V_o)₇₀₀ > pristine TiO₂, which is perfectly consistent with the trend in oxygen vacancy concentration (Fig. S9). We noted that the TON of TiO₂(V_o)₈₀₀ at -0.12 V was determined to be 0.0143, outperforming previously reported oxygen-vacancy rich TiO₂ with a TON value of 0.0105 for photocatalytic dinitrogen fixation [28]. Thus, V_o evidently endowed TiO₂ with improved catalytic efficiency for NRR. The higher the concentration of the oxygen vacancies, the better the activity of the sample for N₂ reduction. We further used electrochemical impedance spectroscopy (EIS) to analyze the effects of oxygen vacancies on NRR. The Nyquist plots in Fig. S10 revealed a smaller charge transfer resistance of TiO₂(V_o)₈₀₀ as compared with TiO₂(V_o)₇₀₀ and TiO₂(V_o)₉₀₀. This implies that increase of V_o in TiO₂ accelerated NRR reaction kinetics.

To examine if there exist interferences from environmental NH₃ that might be in the solution or adsorbed to the laboratory materials when analyzing NRR, we carried out multiple blank and control experiments. As shown in Fig. 3d, very little or no NH₃ is detected by the indophenol blue method in Ar (99.999% purity)-saturated HCl, or with carbon paper electrode (Carbon paper) without TiO₂(V_o)₈₀₀, or with just the background Nafion solution binder (Binder), or at an open circuit potential as a control. These results imply that NH₃ generated is due to electroreduction of dissolved N₂ by the TiO₂ catalyst.

The catalyst stability was evaluated at a constant potential of -0.12 V for cycles. Both the NH₃ FE and the yield rate remained constant during the first 5 cycles and maintained at 5.0% and 2.8 μg_{NH3} h⁻¹ mg_{cat}⁻¹, respectively, after 15 cycles (Fig. 3e). Further alternated electrolysis cycling test between Ar- and N₂-saturated electrolytes indicated that the produced NH₃ was evolved from the feed gas N₂ and can be stable over 5 cycles (Fig. 3f). Chronoamperometry measurements showed that the overall current density is essentially unchanged after over 33 h (Fig. 3g). ESR (Fig. S11a) and XPS (Fig. S11b) analyses of TiO₂(V_o)₈₀₀ after electrolysis revealed the preservation of oxygen vacancies, accounting for the good durability of such V_o-rich TiO₂.

We investigated the impact of N₂ flow rate on NRR. Measurable effect of N₂ flow rate was observed at flow rates below 10 mL min⁻¹ (Fig. 4a), indicating that diffusion is the rate determining step. While this is unlikely the case when the flow rates are higher than 20 mL min⁻¹. Virtually, both NH₃ yield rate and FE were found to retain nearly

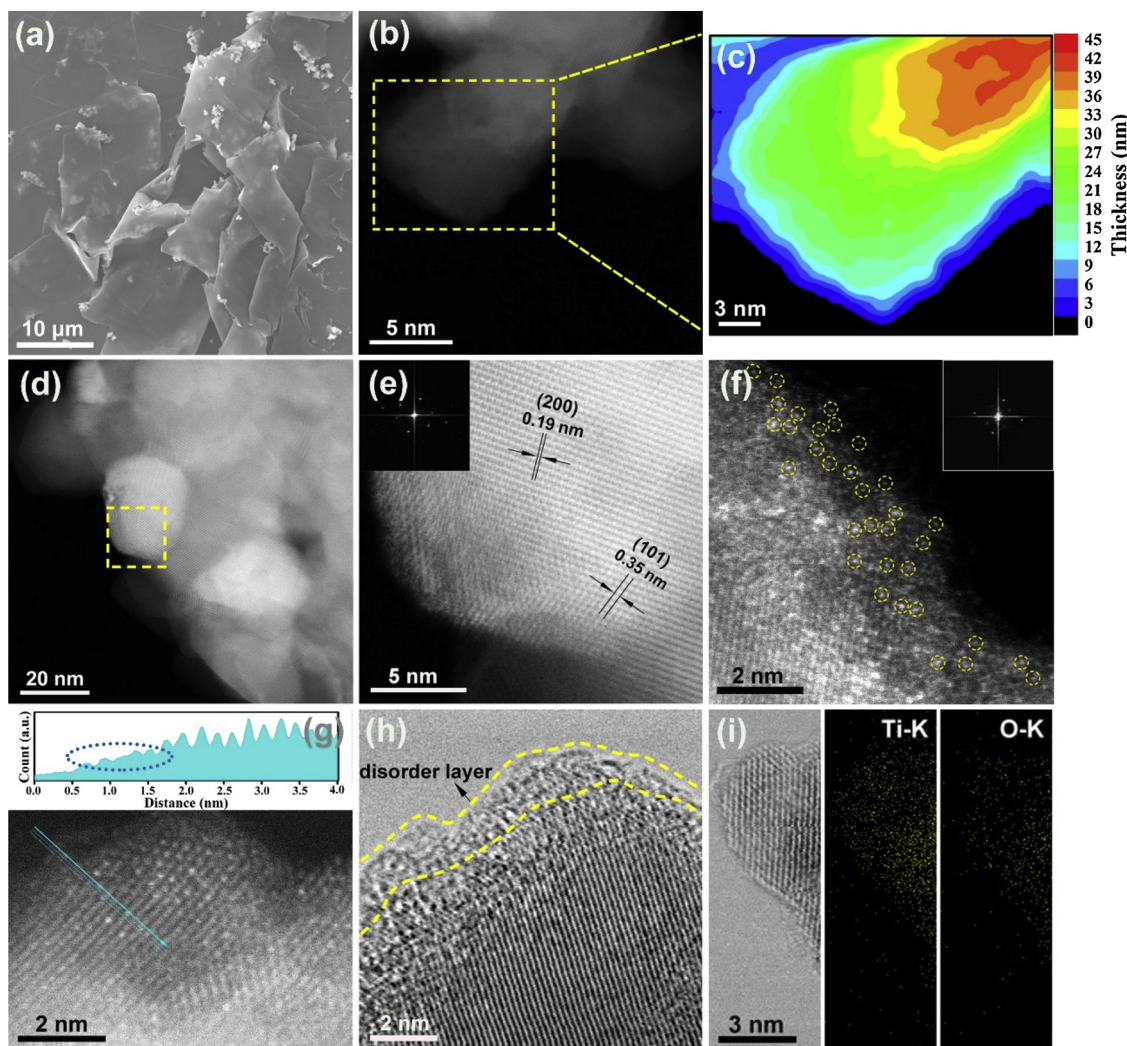


Fig. 2. (a) SEM and (b) aberration-corrected HAADF-STEM images of $\text{TiO}_2(\text{V}_o)_{800}$. (c) Quasi-color image of b, showing the thickness of overlapped flakes. (d) Low-magnification STEM image. (e)–(g) High-resolution STEM images. Image e is the enlarged image of the area encased by the dashed square in d and shows a lattice distance of 0.35 and 0.19 nm, in accordance with the (101) and (200) planes of anatase TiO_2 , respectively. The insets in e and f are corresponding FFT patterns. The upper inset in g displays structural analysis during STEM imaging. Analysis region and orientation are marked in the image. (h) HRTEM image in bright field. (i) STEM image of an individual flake together with EDX mapping images of Ti and O elements.

constant within experimental error. By increasing the electrochemical NRR temperature from 0 to 75 °C, both NH_3 yield rate and FE increased correspondingly (Fig. 4b). The mass transport rate increased at elevated temperatures, whereas the N_2 solubility decreased at higher temperatures. Our results showed that faster kinetics dominated the reaction process at higher temperatures, thus accelerating the NRR. We also explored the effect of electrolyte pH on the NRR. Despite decrease in NH_3 yield rate, improving electrolyte pH resulted in an increase in NH_3 FE, surpassing 20% at $2.5 \leq \text{pH} \leq 3.0$, which may due to the reduction of proton concentration and thus slower hydrogen evolution reaction (Fig. S12).

3.3. Role of oxygen vacancies in TiO_2 for NRR

To gain insight into the key role of oxygen vacancies in NRR, both $\text{TiO}_2(\text{V}_o)_{800}$ and $\text{TiO}_2(\text{V}_o)_{900}$ were treated in O_2 atmosphere at 500 °C for 1 h. This treatment could fill all oxygen vacancies but did not affect the respective crystalline structure of each sample (Fig. S13a). The removal of V_o was corroborated by the absence of ESR signal at $g = 2.003$ (Fig. S13b). We found that the O_2 treated samples showed a dramatic decrease in both NH_3 yield rate and FE (Fig. 4c). Such loss of

NRR activities is plausibly attributed to elimination of the oxygen vacancies, given the preservation of crystalline phase in each case. The anatase $\text{TiO}_2(\text{V}_o)_{800}\text{-O}_2$ exhibited similar NRR performance compared to rutile $\text{TiO}_2(\text{V}_o)_{900}\text{-O}_2$, which is supported by the following DFT calculations. Note that our V_o -rich TiO_2 catalysts outperform commercial P25 and even noble metal catalysts, including 5% Ru/C and 20% Pt/C (Fig. 4c), thereby clearly demonstrating their use as potential electrocatalysts in electrochemical N_2 fixation.

N₂ TPD profiles revealed two desorption peaks located at 110 and 300 °C (Fig. 4d), which could be ascribed to N_2 physisorption and N_2 chemisorption, respectively. It is worth noting that the chemisorbed N_2 desorption peak temperature of $\text{TiO}_2(\text{V}_o)_{800}$ here is 300 °C, higher than 250 or 277 °C reported earlier [31,36], illustrating enhanced electron back-donation effect of V_o sites and thus strengthened activation of N_2 compared with other TiO_2 materials with oxygen vacancies. In comparison, only very weak signals of chemisorbed N_2 on pristine TiO_2 without V_o were detected. Therefore, N_2 chemical adsorption and activation could be greatly facilitated by introduction of oxygen vacancies. As expected, the $\text{TiO}_2(\text{V}_o)_{800}$ with the highest V_o concentration delivers the best NRR activity.

Furthermore, to investigate the role of surface oxygen vacancies in

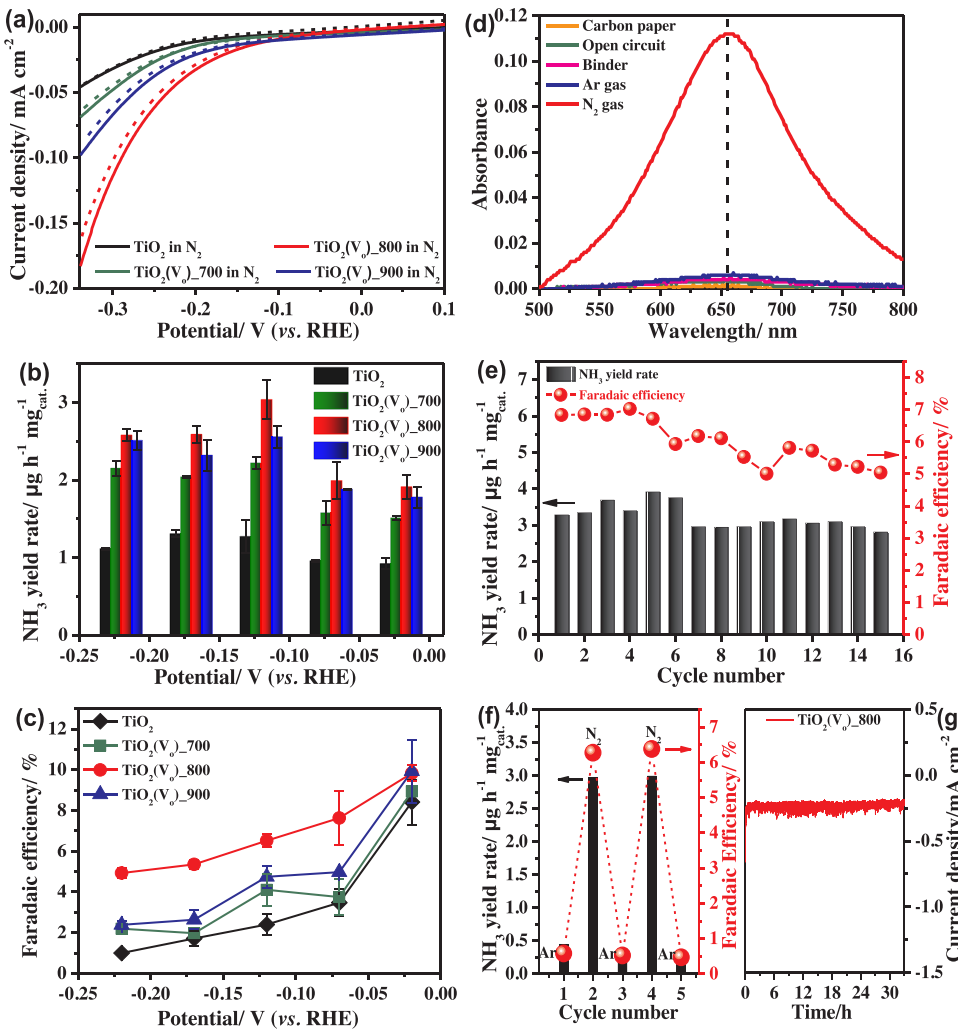


Fig. 3. (a) The LSV results of pristine TiO_2 , $\text{TiO}_2(\text{V}_o)_700$, $\text{TiO}_2(\text{V}_o)_800$, and $\text{TiO}_2(\text{V}_o)_900$ electrodes in Ar- (dashed line) or N_2 - (solid line) saturated 0.1 M HCl solution with a scan rate of 5 mV s^{-1} . (b) The yield rate and (c) FE of NH_3 over pristine TiO_2 , $\text{TiO}_2(\text{V}_o)_700$, $\text{TiO}_2(\text{V}_o)_800$, and $\text{TiO}_2(\text{V}_o)_900$ at various potentials. (d) UV-vis absorption spectra of the electrolyte after electrolysis at -0.12 V for the control experiments with Ar-saturated electrolyte (Ar gas), or without $\text{TiO}_2(\text{V}_o)_800$ catalyst in the absence (Carbon paper) or presence of binder (Binder), or at an open circuit potential (Open circuit). (e) Long-term durability test at -0.12 V over $\text{TiO}_2(\text{V}_o)_800$. (f) NH_3 yield rates and FEs for $\text{TiO}_2(\text{V}_o)_800$ with alternated cycles between Ar- and N_2 -saturated electrolytes at -0.12 V . (g) Chronoamperometry measurements at -0.12 V over $\text{TiO}_2(\text{V}_o)_800$ electrode.

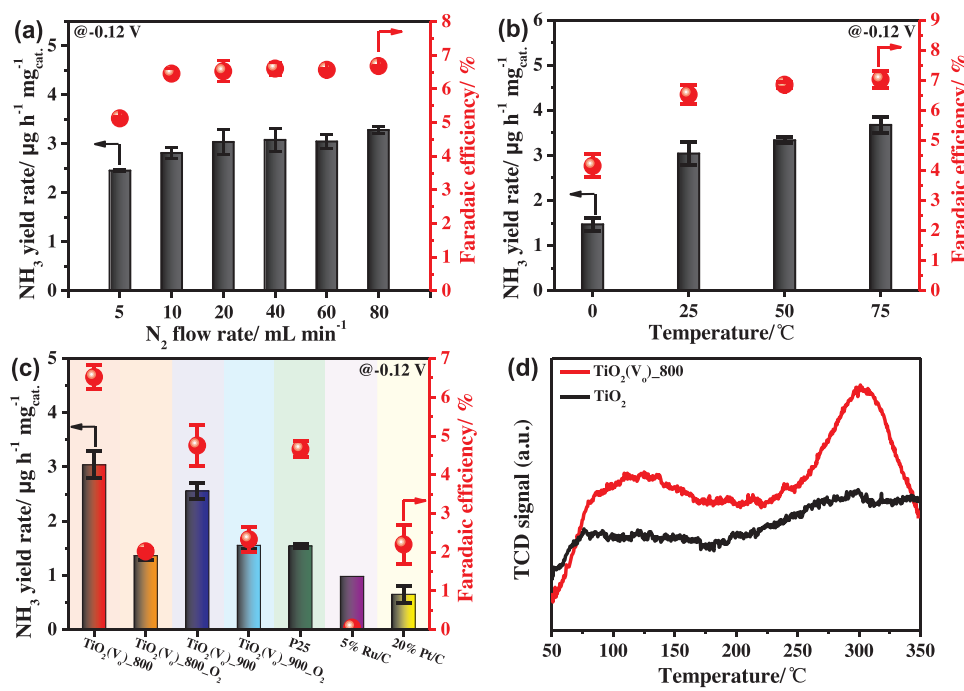


Fig. 4. The NH_3 yield rates and FEs of $\text{TiO}_2(\text{V}_o)_800$ under (a) different N_2 flow rates and (b) various temperatures at -0.12 V . (c) The NH_3 yield rates and FEs of commercial 5% Ru/C, 20% Pt/C, $\text{TiO}_2(\text{V}_o)_800$, $\text{TiO}_2(\text{V}_o)_800\text{-O}_2$, $\text{TiO}_2(\text{V}_o)_900$, $\text{TiO}_2(\text{V}_o)_900\text{-O}_2$, and P25 at -0.12 V . (d) N_2 -TPD profiles of pristine TiO_2 and $\text{TiO}_2(\text{V}_o)_800$.

TiO_2 on catalytic activity for NRR, DFT calculations were performed. The anatase and rutile TiO_2 that are the most dominant crystalline phase in $\text{TiO}_2(\text{V}_o)_800$ and $\text{TiO}_2(\text{V}_o)_900$ were considered. The anatase (101) and rutile (110) facets, the most stable facet in each phase, were taken into account. In addition, among several possible surface oxygen sites, we have considered the most stable vacancy site in each phase as shown in Fig. S14. For notations, we use rutile- V_o and anatase- V_o to denote the most stable surface oxygen vacancy site in rutile and anatase TiO_2 , respectively. The surface oxygen vacancy concentration in both rutile- V_o and anatase- V_o in our calculation model is 25%, similar to that obtained experimentally, i.e., $\text{TiO}_2(\text{V}_o)_800$ (32.2%) and $\text{TiO}_2(\text{V}_o)_900$ (25.6%). Among many possible intermediate reaction steps in NRR, we mainly focused on the potential rate determining step (PDS), that is, the step with the largest free energy requirement. The catalytic activity for NRR was estimated by comparing the free energy change at PDS (ΔG_{PDS}), i.e., thermodynamic overpotential. The optimized structures of the key reaction intermediates for anatase- V_o and rutile- V_o in the lowest free energy requiring pathway are shown in Fig. S15 and Fig. S16, respectively. The calculation details and atomic coordinates of the optimized geometries for reaction intermediates on anatase- V_o and rutile- V_o were presented in Supporting Information.

We found that anatase- V_o and rutile- V_o follow the same reaction pathway for NRR. For both catalysts, the lowest energy pathway is expressed as: $^*\text{N}_2 \rightarrow ^*\text{NNH} \rightarrow ^*\text{NNH}_2 \rightarrow ^*\text{NHNH}_2 \rightarrow ^*\text{NH}_2\text{NH}_2 \rightarrow ^*\text{NH}_2 + \text{NH}_3 \rightarrow ^*\text{NH}_3 + \text{NH}_3 \rightarrow 2\text{NH}_3$, where the proton and electron pair ($\text{H}^+ + \text{e}^-$) in each intermediate is omitted for clarity (Fig. 5, Fig. S15, and Fig. S16). The free energy diagrams for NRR on pristine and oxygen vacancy containing TiO_2 indicate that the surface oxygen vacancies in TiO_2 play a significant role in enhancing the catalytic activity (Fig. 5). For example, the free energy change for the $^*\text{NNH}$ formation ($^*\text{N}_2 + (\text{H}^+ + \text{e}^-) \rightarrow ^*\text{NNH}$), the first electrochemical reduction step, is thermodynamically unfavorable (uphill) over anatase TiO_2 (2.15 eV) and rutile TiO_2 (2.11 eV). By sharp contrast, the surface oxygen vacancies stabilize the $^*\text{NNH}$ species considerably, lowering the associated free energy change notably to 0.42 and 0.74 eV for anatase- V_o and rutile- V_o , respectively. Incidentally, the fact that the calculated ΔG_{PDS} for anatase TiO_2 (2.15 eV) and rutile TiO_2 (2.11 eV) agrees with the small difference in the experimental NH_3 yield rate between $\text{TiO}_2(\text{V}_o)_800\text{-O}_2$ and $\text{TiO}_2(\text{V}_o)_900\text{-O}_2$, indicates the insignificant effect of crystalline phase transformation on catalytic activity (Fig. 4c).

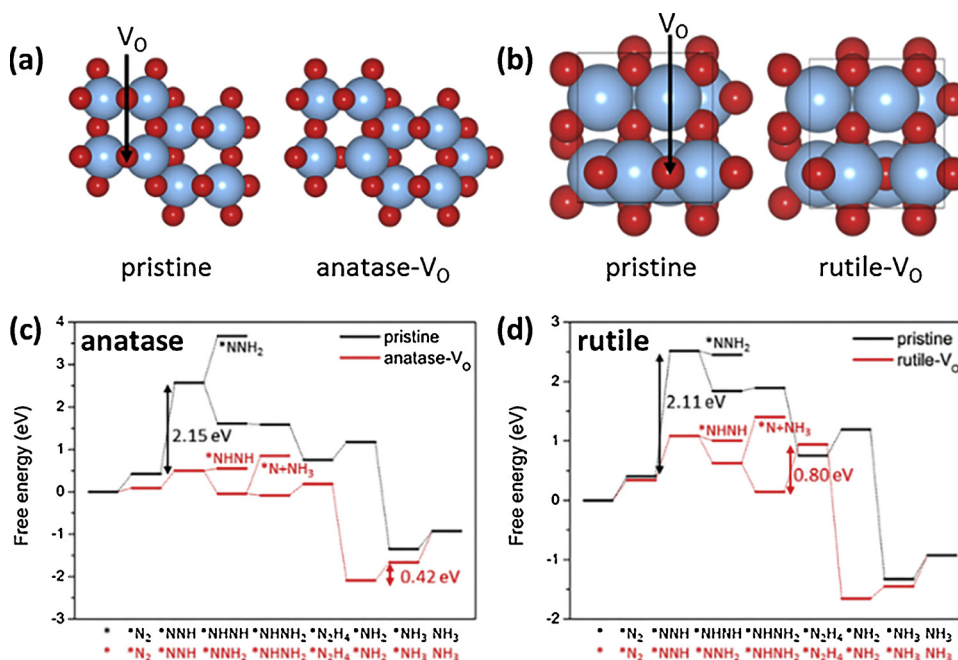
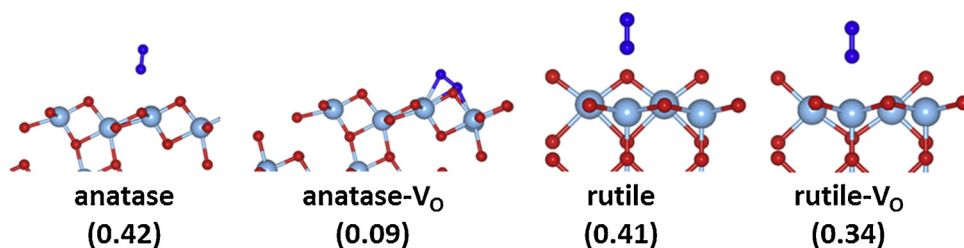


Fig. 5. The optimized geometries (top-view) of pristine and the most stable surface oxygen vacancy containing (a) anatase (101) and (b) rutile (110) facets. The free energy diagram for NRR on pristine and V_o containing (c) anatase (101) and (d) rutile (110) facets. For anatase (101), only the topmost layer is shown for clarity. The sky blue and red balls indicate Ti and O atoms, respectively. The ΔG_{PDS} is shown in c and d. (For interpretation of the references to colour in this figure legend, the reader is referred to the web version of this article).

Due to such a facilitation of the otherwise most difficult first protonation ($^*\text{NNH}$ formation) step, the PDS for anatase- V_o and rutile- V_o in the presence of oxygen vacancies are different from the pristine case with substantially smaller ΔG_{PDS} values. The ΔG_{PDS} for anatase- V_o and rutile- V_o are 0.42 eV ($^*\text{NH}_2 + \text{H}^+ + \text{e}^- \rightarrow ^*\text{NH}_3$) and 0.80 eV ($^*\text{NHNH}_2 + \text{H}^+ + \text{e}^- \rightarrow ^*\text{NH}_2\text{NH}_2$), respectively. Such a dramatic lowering of ΔG_{PDS} in the presence of oxygen vacancies compared to pristine TiO_2 by 1.4–1.7 eV suggests clearly that the surface oxygen vacancies in both the anatase and rutile TiO_2 can improve catalytic activity, as evidenced by the enhanced NH_3 yield rate and NH_3 FE with increase of oxygen vacancies (Fig. 4c).

In addition to ΔG_{PDS} , we found that anatase- V_o can boost N_2 adsorption. The optimized structures of $^*\text{N}_2$ suggest that the N_2 molecule is chemically adsorbed only on anatase- V_o , leading to more negative free energy change of N_2 adsorption ($\Delta G(^*\text{N}_2)$) on anatase- V_o (0.09 eV) compared to other sites (0.34 ~ 0.42 eV) (Fig. 6). This result also matches with the increased chemisorbed N_2 desorption peak on $\text{TiO}_2(\text{V}_o)_800$ in the N_2 -TPD experiments (Fig. 4d).

We also considered the $^*\text{N}_2/^*\text{H}$ selectivity using the difference in adsorption free energies of $^*\text{N}_2$ vs. $^*\text{H}$, since $^*\text{H}$ can hinder NRR by blocking the binding sites for N_2 and catalyze HER. The free energy change of H adsorption ($\Delta G(^*\text{H})$) on anatase- V_o (-0.15 eV) and rutile- V_o (-0.07 eV) are similar, differing by only 0.08 eV (Fig. S17). However, due to the enhanced N_2 adsorption on anatase- V_o , the net difference of $\Delta G(^*\text{N}_2) - \Delta G(^*\text{H})$ for anatase- V_o (0.16 eV) is much smaller than that for rutile- V_o (0.41 eV), indicating that N_2 adsorption will indeed be less hindered by $^*\text{H}$ on anatase- V_o . We further considered the competitive adsorption of H_2O and N_2 at O-vacancy sites, since the H_2O can also block the active sites for NRR. The calculated free energy of H_2O adsorption on anatase- V_o (-0.10 eV) and rutile- V_o (-0.16 eV) are not highly negative, indicating that significant poisoning of O-vacancy sites by H_2O is not expected (Fig. S18). Similar to the $^*\text{N}_2/^*\text{H}$ selectivity, the net difference of $\Delta G(^*\text{N}_2) - \Delta G(^*\text{H}_2\text{O})$ for anatase- V_o (0.19 eV) is much smaller than that for rutile- V_o (0.50 eV). Thus, we expect that N_2 adsorption will be less hindered by $^*\text{H}$ and $^*\text{H}_2\text{O}$ on anatase- V_o , which is the main active site of $\text{TiO}_2(\text{V}_o)_800$. Consequently, we conclude that the improved NH_3 yield rate and FE of $\text{TiO}_2(\text{V}_o)_800$ mainly originate from the significantly lowered ΔG_{PDS} with enhanced N_2 affinity on anatase- V_o , while the effect of crystalline phase transformation is insignificant.



4. Conclusions

In summary, we have shown the possibility of realizing electrochemical synthesis of NH_3 over TiO_2 with abundant oxygen vacancies. An NH_3 production rate of about $3.0 \mu\text{g}_{\text{NH}_3} \text{h}^{-1} \text{mg}_{\text{cat}}^{-1}$ and a faradaic efficiency of up to 6.5% have been simultaneously achieved at an overpotential of 180 mV. The creation of oxygen vacancies was found to significantly promote N_2 adsorption as well as activation of the $\text{N}\equiv\text{N}$ triple bond, favoring NRR. The electrocatalytic performances were further tuned by controlling the concentration of oxygen vacancies. DFT studies indicated that the surface oxygen vacancies of TiO_2 indeed help lower ΔG_{PDS} of NRR dramatically, leading to enhanced electrocatalysis of the NRR. Moreover, the anatase- V_0 sites play an important role in improving the faradaic efficiency of N_2 to NH_3 conversion by increasing N_2 chemisorption relative to $^*\text{H}$. Our results may foster further research on engineering defects of metal oxide (hydroxide) catalysts for electrocatalytic N_2 fixation.

Conflict of interests

Nothing declared.

Acknowledgements

This work was supported by the State Key Laboratory of Organic-Inorganic Composites (No. oic-201503005 and oic-201901001); Beijing Natural Science Foundation (No. 2192039); Beijing National Laboratory for Molecular Sciences (BNLMS20160133); Beijing University of Chemical Technology (XK180301); the State Key Laboratory of Separation Membranes and Membrane Processes (Tianjin Polytechnic University, No. M2-201704); the National Research Foundation of Korea from the Korean Government (NRF-2019M3D3A1A01069099 and NRF-2016M3D1A1021147).

Appendix A. Supplementary data

Supplementary material related to this article can be found, in the online version, at doi:<https://doi.org/10.1016/j.apcatb.2019.117896>.

References

- [1] J. Wang, L. Yu, L. Hu, G. Chen, H.L. Xin, X.F. Feng, Ambient ammonia synthesis via palladium-catalyzed electrohydrogenation of dinitrogen at low overpotential, *Nat. Commun.* 9 (2018) 1795.
- [2] B.C. Cui, J.H. Zhang, S.Z. Liu, X.J. Liu, W. Xiang, L.F. Liu, H.Y. Xin, M.J. Lefler, S. Licht, Electrochemical synthesis of ammonia directly from N_2 and water over iron-based catalysts supported on activated carbon, *Green Chem.* 19 (2017) 298–304.
- [3] B.K. Burgess, D.J. Lowe, Mechanism of molybdenum nitrogenase, *Chem. Rev.* 96 (1996) 2983–3011.
- [4] D. Bao, Q. Zhang, F.L. Meng, H.X. Zhong, M.M. Shi, Y. Zhang, J.M. Yan, Q. Jiang, X.B. Zhang, Electrochemical reduction of N_2 under ambient conditions for artificial N_2 fixation and renewable energy storage using N_2/NH_3 cycle, *Adv. Mater.* 29 (2017) 1604799.
- [5] F. Koleli, T. Ropke, Electrochemical hydrogenation of dinitrogen to ammonia on a polyaniline electrode, *Appl. Catal. B-Environ.* 62 (2006) 306–310.
- [6] H.C. Tao, C. Choi, L.X. Ding, Z. Jiang, Z.S. Han, M.W. Jia, Q. Fan, Y.N. Gao, H.H. Wang, A.W. Robertson, S. Hong, Y. Jung, S.Z. Liu, Z.Y. Sun, Nitrogen fixation by Ru single-atom electrocatalytic reduction, *istryChem* 5 (2019) 204–214.
- [7] L.L. Zhang, L.X. Ding, G.F. Chen, X.F. Yang, H.H. Wang, Ammonia synthesis under ambient conditions: selective electroreduction of dinitrogen to ammonia on black phosphorus nanosheets, *Angew. Chem. Int. Ed.* 58 (2019) 2612–2616.
- [8] H. Cheng, L.X. Ding, G.F. Chen, L.L. Zhang, J. Xue, H.H. Wang, Molybdenum carbide nanodots enable efficient electrocatalytic nitrogen fixation under ambient conditions, *Adv. Mater.* 30 (2018) 1803694.
- [9] G.F. Chen, X.R. Cao, S.Q. Wu, X.Y. Zeng, L.X. Ding, M. Zhu, H.H. Wang, Ammonia electrosynthesis with high selectivity under ambient conditions via a Li^+ incorporation strategy, *J. Am. Chem. Soc.* 139 (2017) 9771–9774.
- [10] Y.R. Luo, G.F. Chen, L. Ding, X.Z. Chen, L.X. Ding, H.H. Wang, Efficient electrocatalytic N_2 fixation with MXene under ambient conditions, *Joule* 3 (2019) 279–289.
- [11] Q. Fan, C. Choi, C. Yan, Y. Liu, J. Qiu, S. Hong, Y. Jung, Z. Sun, High-yield production of few-layer boron nanosheets for efficient electrocatalytic N_2 reduction, *Chem. Commun.* 55 (2019) 4246–4249.
- [12] D.B. Kayan, F. Koleli, Simultaneous electrocatalytic reduction of dinitrogen and carbon dioxide on conducting polymer electrodes, *Appl. Catal. B-Environ.* 181 (2016) 88–93.
- [13] D. Zhu, L.H. Zhang, R.E. Ruther, R.J. Hamers, Photo-illuminated diamond as a solid-state source of solvated electrons in water for nitrogen reduction, *Nat. Mater.* 12 (2013) 836–841.
- [14] S.M. Sun, Q. An, W.Z. Wang, L. Zhang, J.J. Liu, W.A. Goddard, Efficient photocatalytic reduction of dinitrogen to ammonia on bismuth monoxide quantum dots, *J. Mater. Chem. A Mater. Energy Sustain.* 5 (2017) 201–209.
- [15] S.H. Cao, H. Chen, F. Jiang, X. Wang, Nitrogen photofixation by ultrathin amine-functionalized graphitic carbon nitride nanosheets as a gaseous product from thermal polymerization of urea, *Appl. Catal. B-Environ.* 224 (2018) 222–229.
- [16] C.L. Xiao, L. Zhang, K.F. Wang, H.P. Wang, Y.Y. Zhou, W.Z. Wang, A new approach to enhance photocatalytic nitrogen fixation performance via phosphate-bridge: a case study of $\text{SiW}_{12}/\text{K-C}_3\text{N}_4$, *Appl. Catal. B-Environ.* 239 (2018) 260–267.
- [17] P.X. Qiu, C.M. Xu, N. Zhou, H. Chen, F. Jiang, Metal-free black phosphorus nanosheets-decorated graphitic carbon nitride nanosheets with C-P bonds for excellent photocatalytic nitrogen fixation, *Appl. Catal. B-Environ.* 221 (2018) 27–35.
- [18] S.M. Sun, X.M. Li, W.Z. Wang, L. Zhang, X. Sun, Photocatalytic robust solar energy reduction of dinitrogen to ammonia on ultrathin MoS_2 , *Appl. Catal. B-Environ.* 200 (2017) 323–329.
- [19] X. Cui, C. Tang, Q. Zhang, A review of electrocatalytic reduction of dinitrogen to ammonia under ambient conditions, *Adv. Energy Mater.* (2018) 1800369.
- [20] N. Cao, G.F. Zheng, Aqueous electrocatalytic N_2 reduction under ambient conditions, *Nano Res.* 11 (2018) 2992–3008.
- [21] Z. Sun, T. Ma, H. Tao, Q. Fan, B. Han, Fundamentals and challenges of electrochemical CO_2 reduction using two-dimensional materials, *istryChem* 3 (2017) 560–587.
- [22] L.J. Liu, Y.Q. Jiang, H.L. Zhao, J.T. Chen, J.L. Cheng, K.S. Yang, Y. Li, Engineering coexposed (001) and (101) facets in oxygen-deficient TiO_2 nanocrystals for enhanced CO_2 photoreduction under visible light, *ACS Catal.* 6 (2016) 1097–1108.
- [23] Z.G. Geng, X.D. Kong, W.W. Chen, H.Y. Su, Y. Liu, F. Cai, G.X. Wang, J. Zeng, Oxygen vacancies in ZnO nanosheets enhance CO_2 electrochemical reduction to CO , *Angew. Chem. Int. Ed.* 57 (2018) 6054–6059.
- [24] Z. Sun, N. Talreja, H. Tao, J. Texter, M. Muhler, J. Strunk, J. Chen, Catalysis of carbon dioxide photoreduction on nanosheets: fundamentals and challenges, *Angew. Chem. Int. Ed.* 57 (2018) 7610–7627.
- [25] Y.N. Liu, C.L. Miao, P.F. Yang, Y.F. He, J.T. Feng, D.Q. Li, Synergistic promotional effect of oxygen vacancy-rich ultrathin TiO_2 and photochemical induced highly dispersed Pt for photoreduction of CO_2 with H_2O , *Appl. Catal. B-Environ.* 244 (2019) 919–930.
- [26] M.C. Tsai, T.T. Nguyen, N.G. Akalework, C.J. Pan, J. Rick, Y.F. Liao, W.N. Su, B.J. Hwang, Interplay between molybdenum dopant and oxygen vacancies in a TiO_2 support enhances the oxygen reduction reaction, *ACS Catal.* 6 (2016) 6551–6559.
- [27] J. Li, H. Zhou, H. Zhuo, Z.Z. Wei, G.L. Zhuang, X. Zhong, S.W. Deng, X.N. Li, J.G. Wang, Oxygen vacancies on TiO_2 promoted the activity and stability of supported Pd nanoparticles for the oxygen reduction reaction, *J. Mater. Chem. A Mater. Energy Sustain.* 6 (2018) 2264–2272.
- [28] H. Hirakawa, M. Hashimoto, Y. Shiraishi, T. Hirai, Photocatalytic conversion of nitrogen to ammonia with water on surface oxygen vacancies of titanium dioxide, *J. Am. Chem. Soc.* 139 (2017) 10929–10936.
- [29] H. Li, J. Shang, Z.H. Ai, L.Z. Zhang, Efficient visible light nitrogen fixation with BiOBr nanosheets of oxygen vacancies on the exposed (001) facets, *J. Am. Chem. Soc.* 137 (2015) 6393–6399.
- [30] Y. Zhao, Y. Zhao, G.I.N. Waterhouse, L. Zheng, X. Cao, F. Teng, L.Z. Wu, C.H. Tung, D. O'Hare, T. Zhang, Layered-double-hydroxide nanosheets as efficient visible-light-driven photocatalysts for dinitrogen fixation, *Adv. Mater.* 29 (2017) 1703828.

[31] C.C. Li, T. Wang, Z.J. Zhao, W.M. Yang, J.F. Li, A. Li, Z.L. Yang, G.A. Ozin, J.L. Gong, Promoted fixation of molecular nitrogen with surface oxygen vacancies on plasmon-enhanced TiO_2 photoelectrodes, *Angew. Chem. Int. Ed.* 57 (2018) 5278–5282.

[32] Z.Y. Sun, X. Huang, M. Muhler, W.G. Schuhmann, E. Ventosa, A carbon-coated TiO_2 (B) nanosheet composite for lithium ion batteries, *Chem. Commun.* 50 (2014) 5506–5509.

[33] L.D. Li, J.Q. Yan, T. Wang, Z.J. Zhao, J. Zhang, J.L. Gong, N.J. Guan, Sub-10 nm rutile titanium dioxide nanoparticles for efficient visible-light-driven photocatalytic hydrogen production, *Nat. Commun.* 6 (2015) 5881.

[34] H.Y. Gao, G.X. Hu, J. Sui, C. Mu, W.F. Shangguan, M. Kong, S.T. Wei, Scalable preparation of defect-rich free-standing TiO_2 sheets with visible-light photocatalytic activity, *Appl. Catal. B-Environ.* 226 (2018) 337–345.

[35] B.J. Morgan, G.W. Watson, Intrinsic n-type defect formation in TiO_2 : a comparison of rutile and anatase from GGA plus U calculations, *J. Phys. Chem. C* 114 (2010) 2321–2328.

[36] J.H. Yang, Y.Z. Guo, R.B. Jiang, F. Qin, H. Zhang, W.Z. Lu, J.F. Wang, J.C. Yu, High efficiency "working-in-tandem" nitrogen photofixation achieved by assembling plasmonic gold nanocrystals on ultrathin titania nanosheets, *J. Am. Chem. Soc.* 140 (2018) 8497–8508.

[37] A. Naldoni, M. Allieta, S. Santangelo, M. Marelli, F. Fabbri, S. Cappelli, C.L. Bianchi, R. Psaro, V. Dal Santo, Effect of nature and location of defects on bandgap narrowing in black TiO_2 nanoparticles, *J. Am. Chem. Soc.* 134 (2012) 7600–7603.

[38] J.L. Li, M. Zhang, Z.J. Guan, Q.Y. Li, C.Q. He, J.J. Yang, Synergistic effect of surface and bulk single-electron-trapped oxygen vacancy of TiO_2 in the photocatalytic reduction of CO_2 , *Appl. Catal. B-Environ.* 206 (2017) 300–307.

[39] X.Y. Pan, M.Q. Yang, X.Z. Fu, N. Zhang, Y.J. Xu, Defective TiO_2 with oxygen vacancies: synthesis, properties and photocatalytic applications, *Nanoscale* 5 (2013) 3601–3614.

[40] Y.M. Liu, Y. Su, X. Quan, X.F. Fan, S. Chen, H.T. Yu, H.M. Zhao, Y.B. Zhang, J.J. Zhao, Facile ammonia synthesis from electrocatalytic N_2 reduction under ambient conditions on N-doped porous carbon, *ACS Catal.* 8 (2018) 1186–1191.

[41] G.W. Watt, J.D. Chrisp, A spectrophotometric method for the determination of hydrazine, *Anal. Chem.* 24 (1952) 2006–2008.

[42] L. Yang, T.W. Wu, R. Zhang, H. Zhou, L. Xia, X.F. Shi, H.G. Zheng, Y.N. Zhang, X.P. Sun, Insights into defective TiO_2 in electrocatalytic N_2 reduction: combining theoretical and experimental studies, *Nanoscale* 11 (2019) 1555–1562.

[43] D.H. Thomas, M. Rey, P.E. Jackson, Determination of inorganic cations and ammonium in environmental waters by ion chromatography with a high-capacity cation-exchange column, *J. Chromatogr. A* 956 (2002) 181–186.

[44] J. Liu, M.S. Kelley, W.Q. Wu, A. Banerjee, A.P. Douvalis, J.S. Wu, Y.B. Zhang, G.C. Schatz, M.G. Kanatzidis, Nitrogenase-mimic iron-containing chalcogels for photochemical reduction of dinitrogen to ammonia, *Proc. Natl. Acad. Sci. U. S. A.* 113 (2016) 5530–5535.

[45] V. Kordali, G. Kyriacou, C. Lambrou, Electrochemical synthesis of ammonia at atmospheric pressure and low temperature in a solid polymer electrolyte cell, *Chem. Commun.* (2000) 1673–1674.

[46] K. Kim, N. Lee, C.Y. Yoo, J.N. Kim, H.C. Yoon, J.I. Han, Communication-electrochemical reduction of nitrogen to ammonia in 2-propanol under ambient temperature and pressure, *J. Electrochem. Soc.* 163 (2016) F610–F612.

[47] M.M. Shi, D. Bao, S.J. Li, B.R. Wulan, J.M. Yan, Q. Jiang, Anchoring PdCu amorphous nanocluster on graphene for electrochemical reduction of N_2 to NH_3 under ambient conditions in aqueous solution, *Adv. Energy Mater.* 8 (2018) 1800124.

[48] S.M. Chen, S. Perathoner, C. Ampelli, C. Mebrahtu, D.S. Su, G. Centi, Electrocatalytic synthesis of ammonia at room temperature and atmospheric pressure from water and nitrogen on a carbon-nanotube-based electrocatalyst, *Angew. Chem. Int. Ed.* 56 (2017) 2699–2703.